Carbon cage isomers and magnetic Dy···Dy interactions in $Dy_2O@C_{88}$ and $Dy_2C_2@C_{88}$ metallofullerenes

Wei Yang,[a,b#] Georgios Velkos,[a#] Svetlana Sudarkova,[a] Bernd Büchner,[a] Stanislav M. Avdoshenko,*[a] Fupin Liu,*[a] Alexey A. Popov,*[a] Ning Chen*[b]

Supporting Information

Experimental details

X-ray diffraction. Single crystal X-ray diffraction data collection was carried out at 100 K at the BESSY storage ring (BL14.2, Berlin-Adlershof, Germany).[1] XDSAPP2.0 suite was employed for data processing.[2, 3] The structure was solved by direct methods and refined by SHELXL-2018.[4] Hydrogen atoms were added geometrically and refined with a riding model.

Mass spectrometry: Laser desorption/ionization time-of-flight (MALDI-TOF) mass-spectra were measured with a Bruker autoflex mass-spectrometer.

UV-Vis spectrometry: UV-vis-NIR absorption spectra were measured in toluene solution at room temperature with Shimadzu 3100 spectrophotometer.

IR spectrometry: IR spectra were measured in transmission mode using Hyperion FTIR microscope attached to Vertex 80 FTIR spectrometer (Bruker). Samples were drop-casted on KBr single-crystalline substrate and dried under vacuum.

Magnetic measurements. DC magnetic measurements of powder samples were performed using a Quantum Design VSM MPMS3 magnetometer. The samples were prepared for measurements by drop-casting from CS_2 solution on quartz holder. Magnetic simulations and fitting were performed using PHI code.[5]

DFT computation. DFT optimization of $Y_2O@C_{88}$ and $Y_2C_2@C_{88}$ isomers and calculations of IR spectra were performed at the PBE/TZ2P level using Priroda code and SBK-type ECP for Y atoms.[6, 7] For CASSCF calculations, the optimized structures were then re-optimized with Dy instead of Y at the PBE-D/PAW level using the VASP code and recommended pseudopotentials with f-shell in-core treatment.[8-12]

CASSCF calculations. *Ab initio* energies and wave functions of CF multiplets for the $DyYO@C_{88}$ and $DyYC_2@C_{88}$ molecules have been calculated at the CASSCF/SO-RASSI level of theory using the quantum chemistry package OpenMOLCAS.[13] The single ion LF-parameters were calculated based on ab initio data with the use of SINGLE_ANISO module.[14]

Synthesis and isolation of metallofullerenes

Dy_2O-clusterfullerenes were synthesized by a modified Krätschmer-Huffman DC arc-discharge method. The carbon rod filled with 1.27 g of Dy_2O_3 powder and 2.3 g of graphite powder (molar ratio of Dy/C = 1:24) was vaporized under a He/CO_2 atmosphere (200 Torr of helium and 20 Torr of CO_2). The soot was collected and refluxed in carbon disulfide (CS_2) under an argon atmosphere for 12 h. Totally, 200 rods were vaporized and ca. 4.0 g crude fullerene extract was obtained (ca. 20 mg per rod). The crude extract was treated with $TiCl_4$, which removed most of the empty fullerenes (Figure S1). Dy_2O-clusterfullerenes were isolated and purified by multistage high-performance liquid chromatography (HPLC) as shown in Fig. S2, giving ca. 0.5 mg **Dy_2O-I**, 0.3 mg **Dy_2O-II** and 0.4 mg **Dy_2O-III** in the end.

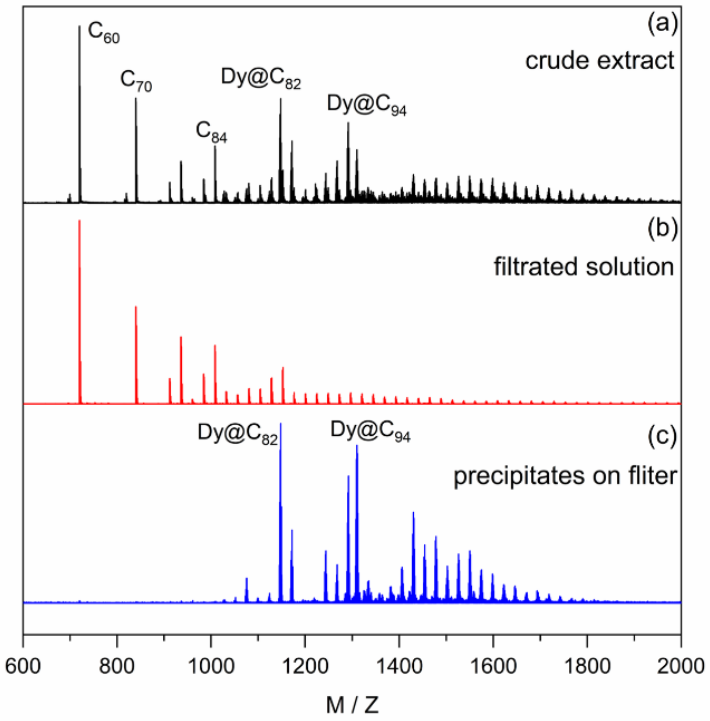

Figure S1. MALDI-TOF (positive ion mode) of (a) crude extract, (b) filtered solution, and (c) precipitates on the filter (complex with $TiCl_4$) for Dy-metallofullerenes.

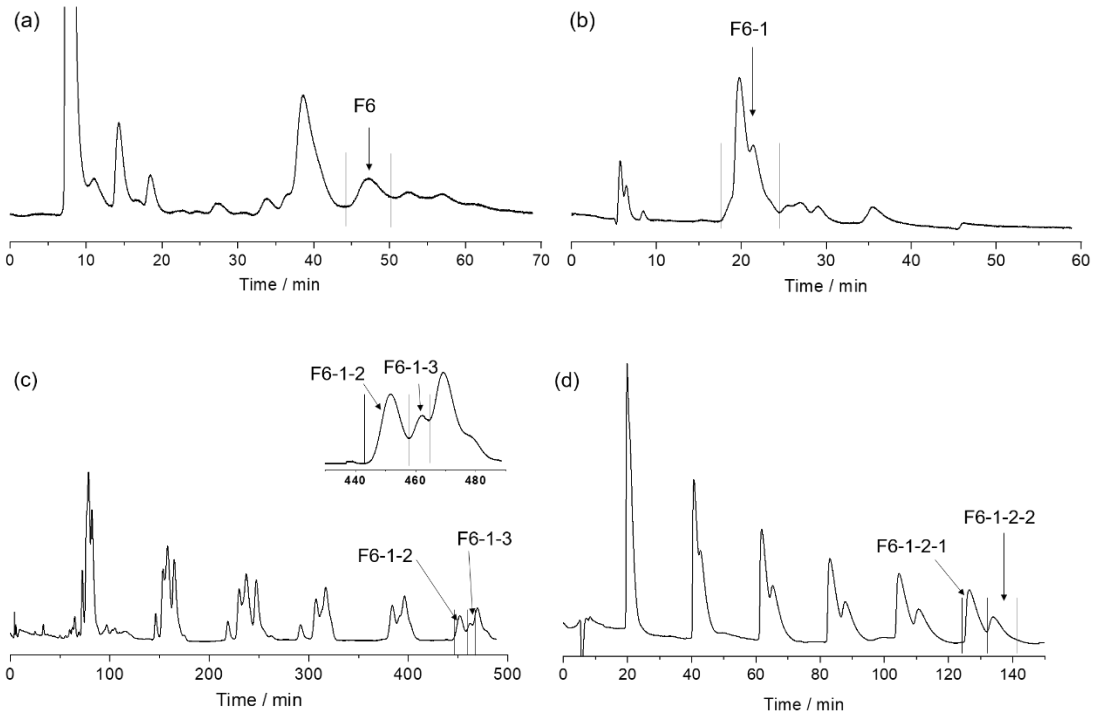

Figure S2. HPLC separation of $Dy_2O@C_{88}$. (a) The first stage HPLC chromatogram of extract recovered from $TiCl_4$ complex on a Buckyprep-M column (Φ = 25 mm × 250 mm, flow rate 10 mL/min) and (b) the second stage HPLC chromatogram of fraction F6 on a Buckyprep-D column (Φ = 10 mm × 250 mm, flow rate 4 mL/min). c) the third stage HPLC chromatogram of fraction F6-1 on a Buckyprep column (Φ = 10 mm × 250 mm, flow rate 4 mL/min). Fraction F6-1-3 is **$Dy_2O@C_{88}$-III**. Insert is enlarged part of HPLC with retention from 430-490min. d) the fourth stage HPLC chromatogram of fraction F6-1-2 on a Buckyprep-D column (Φ = 10 mm × 250 mm, flow rate 4 mL/min). Fraction F6-1-2-1 and F6-1-2-2 were **$Dy_2O@C_{88}$-I** and **$Dy_2O@C_{88}$-II,** respectively. The HPLC conditions were: eluent = toluene; detecting wavelength = 310 nm.

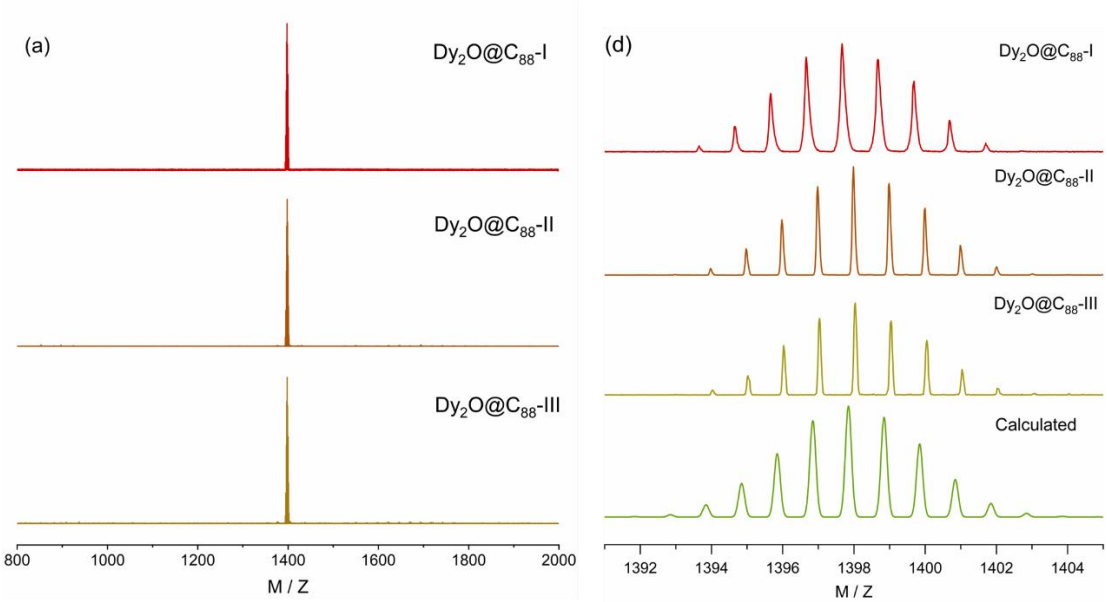

Figure S3. MALDI-TOF of $Dy_2O@C_{88}$ (positive ion mode) with isotopic distribution of main peaks.

Dy_2C_2-clusterfullrenes were synthesized by a similar arc-discharge process. The carbon rod filled with 1.67 g of Dy_2O_3 powder and 0.83 g of graphite powder (molar ratio of Dy/C = 1:7.5) was vaporized under a He/N_2 atmosphere (180 mbar/10 mbar). The soot was collected and refluxed in carbon disulfide (CS_2) under an argon atmosphere for 12 h. Totally, 100 rods were vaporized and ca. 5 g crude fullerene extract was obtained (ca. 50 mg per rod). CS_2 crude extract was dried and re-dissolve in toluene. The crude toluene solution was reacted with dried diamino silica gel (DASG). Empty fullerenes, monometallofullerenes and Dy_2C_2-clusterfullerenes reacted with amino groups and were trapped by DASG, whereas less reactive $Dy_3N@C_{2n}$ clusterfullerenes mainly remained in solution (filtered solution). The DASG with immobilized fullerenes was then filtered and washed with CS_2, which resulted in the release of $Dy_2C_2@C_{2n}$, whereas empty fullerenes and monometallofullerenes remained trapped (Figure S4). Two isomers of $Dy_2C_2@C_{88}$ were isolated and purified by multistage high-performance liquid chromatography (HPLC) as shown in Fig. S5, giving ca. 0.4 mg **Dy_2C_2-I** and 0.2 **mg Dy_2C_2-II** in the end.

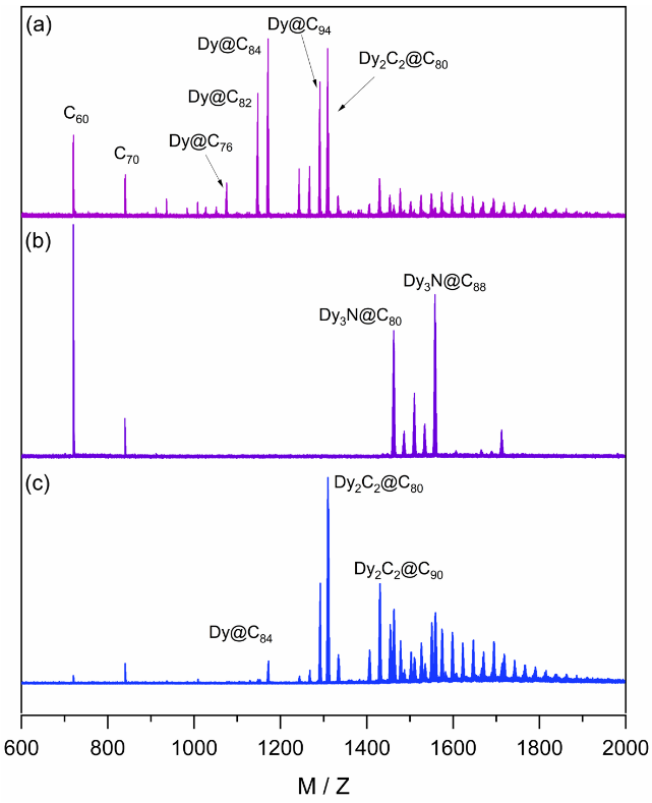

Figure S4. MALDI-TOF (positive ion mode) of (a) crude toluene solution, (b) filtered solution, and (c) CS_2 wash solution

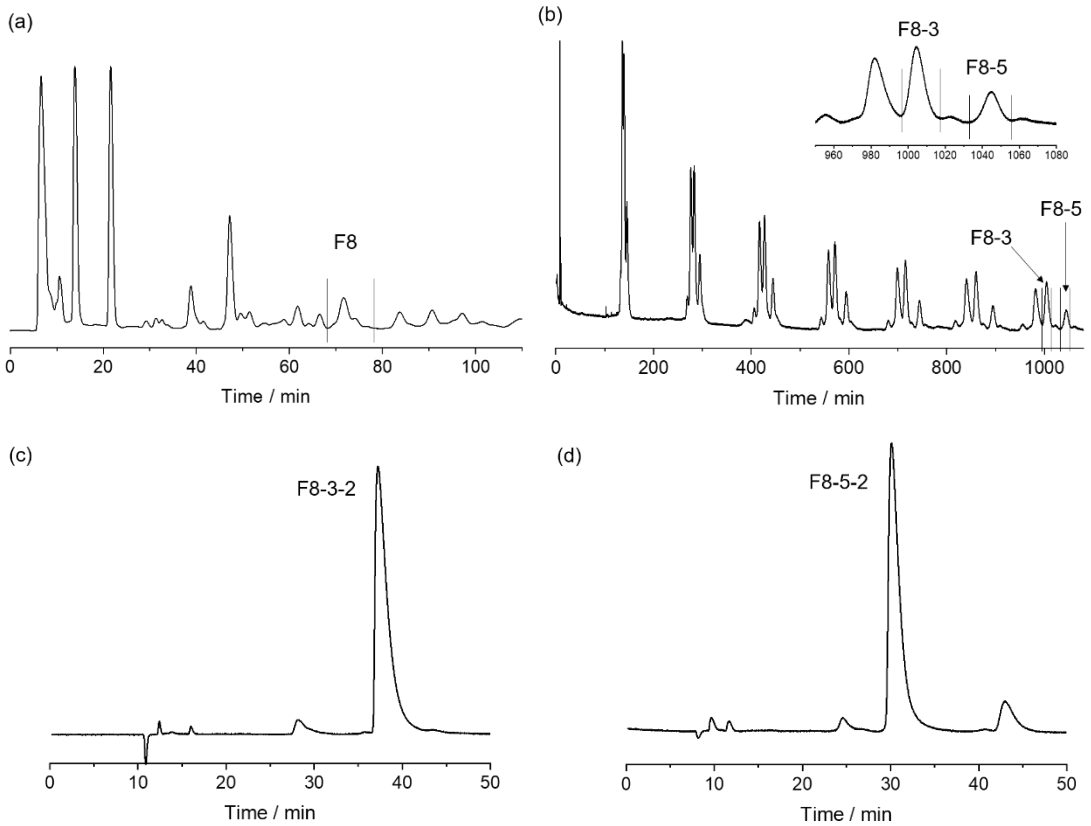

Figure S5. HPLC separation of $Dy_2C_2@C_{88}$. a) The first stage HPLC chromatogram of extract recovered from DASG on a 2×Buckyprep column (Φ = 10 mm × 250 mm, flow rate 5 mL/min) and b) the second stage HPLC chromatogram of fraction F8 on a Buckyprep column (Φ = 10 mm × 250 mm, flow rate 2 mL/min). c-d) the third stage HPLC chromatogram of fraction F8-3 and F8-5 on a Buckyprep-D column (Φ = 10 mm × 250 mm, flow rate 2 mL/min). Fraction F8-3-2 is **$Dy_2C_2@C_{88}$-I** Fraction F8-5-2 is **$Dy_2C_2@C_{88}$-II**. The HPLC conditions were: eluent = toluene; detecting wavelength = 310 nm.

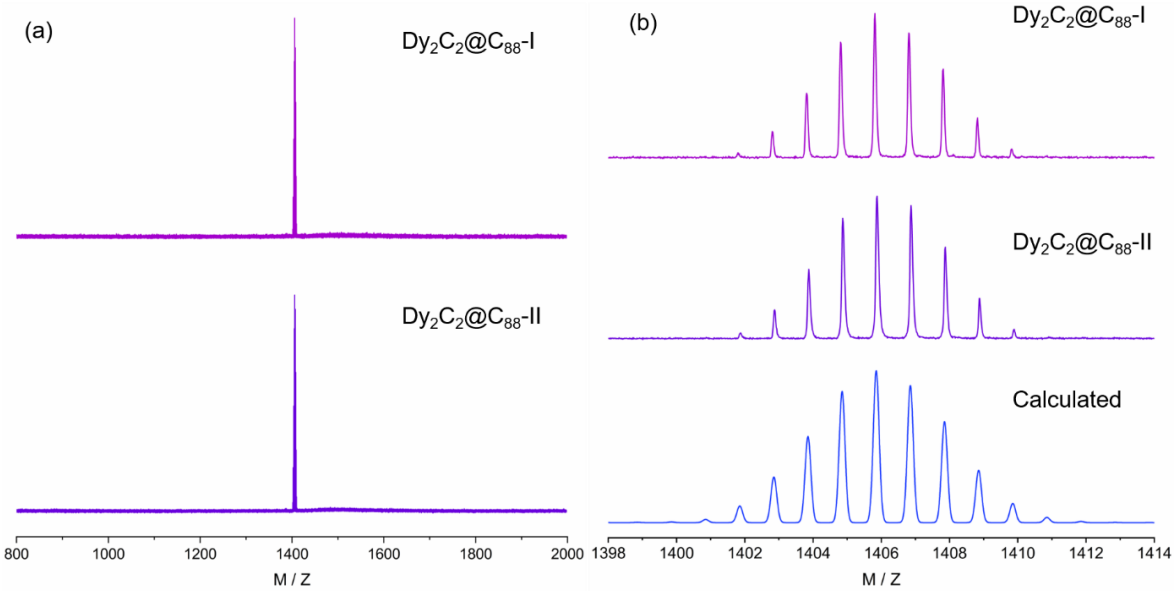

Figure S6. MALDI-TOF of of $Dy_2C_2@C_{88}$ (positive ion mode) with isotopic distribution of main peaks.

Single-crystal X-ray diffraction

Table S1. Crystal data

Crystal	$Dy_2O@C_1(26)$-$C_{88}\cdot NiOEP\cdot C_6H_6\cdot C_7H_8$	$Dy_2C_2@C_s(32)$-$C_{88}\cdot NiOEP\cdot C_6H_6$	$Dy_2C_2@D_2(35)$-$C_{88}\cdot NiOEP\cdot 2C_7H_8$	$Dy_2O@D_2(35)$-$C_{88}\cdot NiOEP\cdot 2C_7H_8$
Formula	$C_{137}H_{58}Dy_2N_4NiO$	$C_{137}H_{50}Dy_2N_4Ni$	$C_{140}H_{60}Dy_2N_4Ni$	$C_{138}H_{60}Dy_2N_4NiO$
Formula weight	2159.58	2135.52	2181.63	2173.61
Color, habit	Black, block	Black, block	Black, block	Black, block
Crystal system	monoclinic	monoclinic	monoclinic	monoclinic
Space group	*C*2/*m*	$P2_1/c$	*C*2/*m*	*C*2/*m*
***a*, Å**	25.340(5)	19.970(4)	25.170(5)	25.220(5)
***b*, Å**	15.220(3)	15.490(3)	15.360(3)	15.330(3)
***c*, Å**	20.350(4)	25.370(5)	20.670(4)	20.540(4)
***α*, deg**	90	90	90	90
***β*, deg**	93.77(3)	93.72(3)	94.58(3)	94.40(3)
***γ*, deg**	90	90	90	90
Volume, Å^3	7831(3)	7831(3)	7966(3)	7918(3)
Z	4	4	4	4
***T*, K**	100	100	100	100
Radiation (λ, Å)	Synchrotron Radiation (0.7999)	Synchrotron Radiation (0.7999)	Synchrotron Radiation (0.77977)	Synchrotron Radiation (0.77977)
Unique data (R_{int})	11878 (0.0333)	12108 (0.1093)	12482 (0.0439)	13345 (0.0583)
Parameters	1143	1397	1200	1133
Restraints	1377	1441	1682	1649
Observed data ($I > 2\sigma(I)$)	11503	7745	12347	12948
R_1^a (observed data)	0.0485	0.1286	0.0638	0.1104
wR_2^b (all data)	0.1313	0.3999	0.1837	0.3152
CCDC NO.	2175825	2175826	2175827	2175828

[a]For data with $I > 2\sigma(I)$, $R_1 = \frac{\sum||F_o|-|F_c||}{\sum|F_o|}$. [b]For all data, $wR_2 = \sqrt{\frac{\sum\left[w\left(F_o^2-F_c^2\right)^2\right]}{\sum\left[w\left(F_o^2\right)^2\right]}}$.

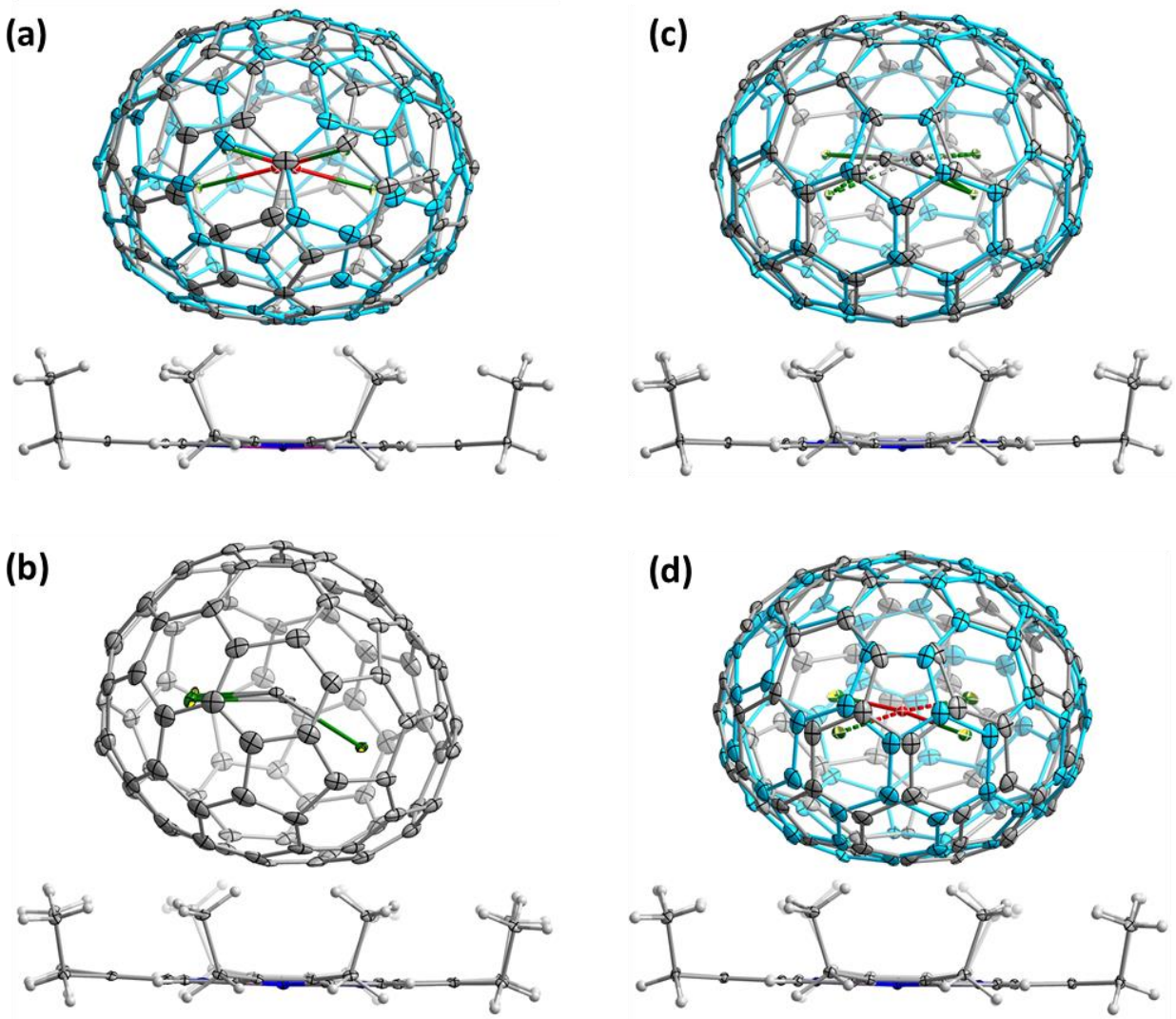

Figure S7. SC-XRD structures of Dy-EMFs co-crystallized with NiOEP. (a) $Dy_2O@C_1(26)$-C_{88}; (b) $Dy_2C_2@C_s(32)$-C_{88}; (c) $Dy_2C_2@D_2(35)$-C_{88}; (d) $Dy_2O@D_2(35)$-C_{88}. In each figure, coordination of the fullerene with the major site of the endohedral cluster to NiOEP is shown. When two fullerene cage enantiomers overlay, they are shown in grey and blue. Only the main cluster site (and its symmetry replica) is shown for each fullerene.

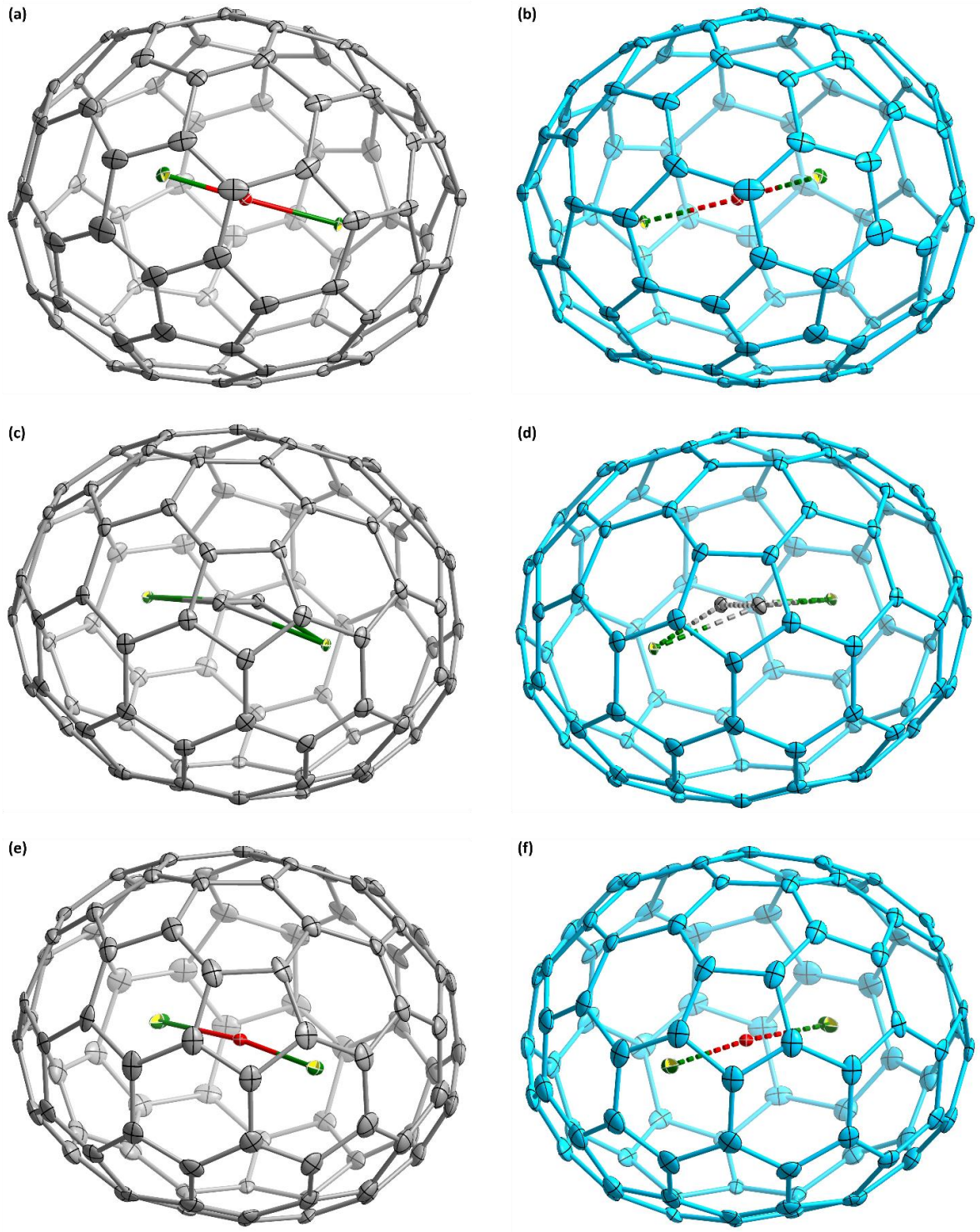

Figure S8. SC-XRD structures of Dy-EMFs co-crystallized with NiOEP. (a, b) $Dy_2O@C_1(26)$-C_{88}; (c, d) $Dy_2C_2@D_2(35)$-C_{88}; (e, f) $Dy_2O@D_2(35)$-C_{88}. Both enantiomers in the structures are shown separately. Only the main cluster site is shown for each fullerene enantiomer.

DFT survey of stable conformers

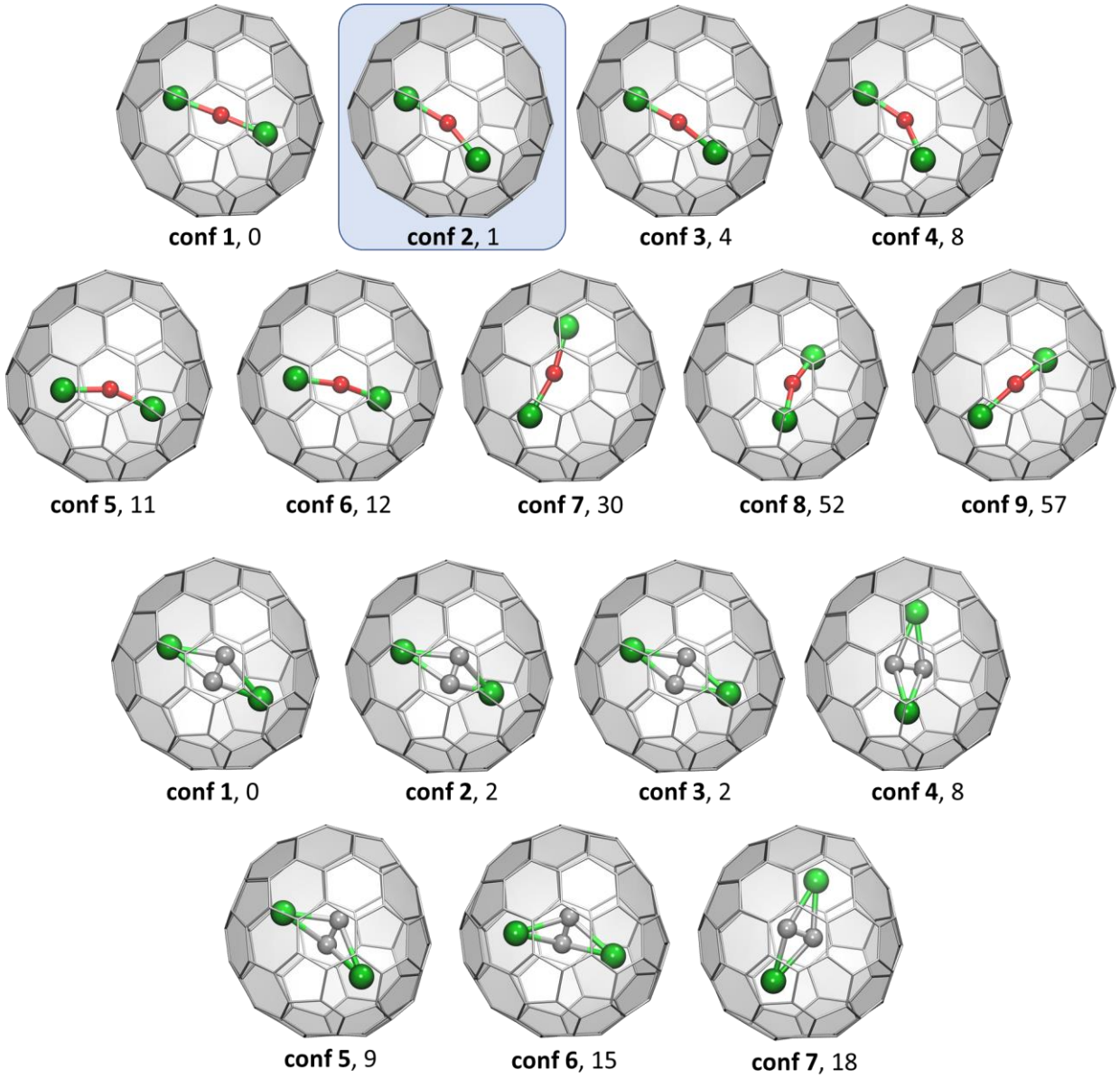

Figure S9a. DFT-optimized molecular structures of unique conformers of $Y_2O@C_1(26)\text{-}C_{88}$ and $Y_2C_2@C_1(26)\text{-}C_{88}$ with their relative energies (the number after comma, in kJ mol^{-1}). The conformer of $Y_2O@C_{88}$ corresponding to the site with the highest occupancy in SC-XRD structure of $Dy_2O@C_1(26)\text{-}C_{88}$ is highlighted with light-blue background.

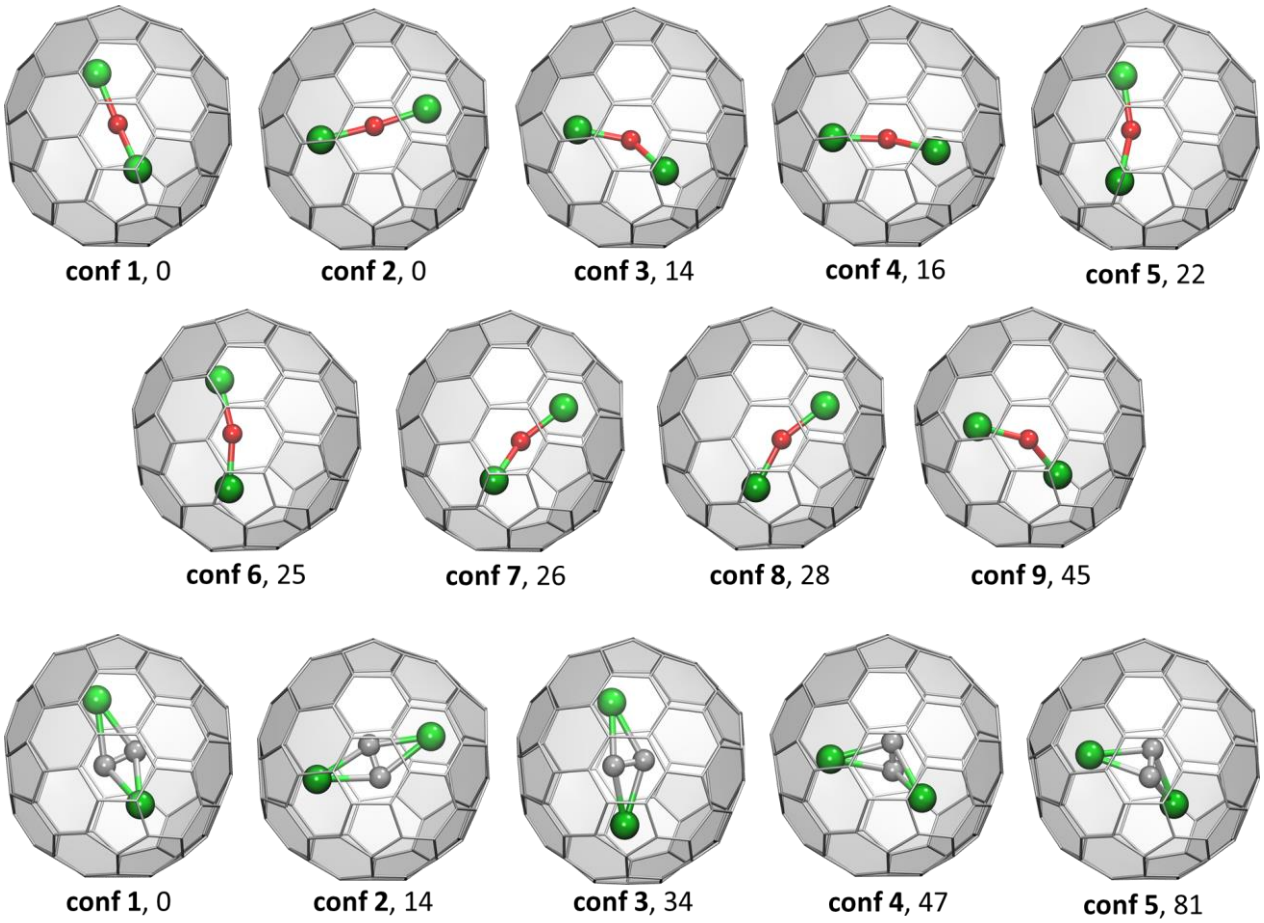

Figure S9b. DFT-optimized molecular structures of unique conformers of $Y_2O@C_1(30)$-C_{88} and $Y_2C_2@C_1(30)$-C_{88} with their relative energies (the number after comma, in kJ mol^{-1}).

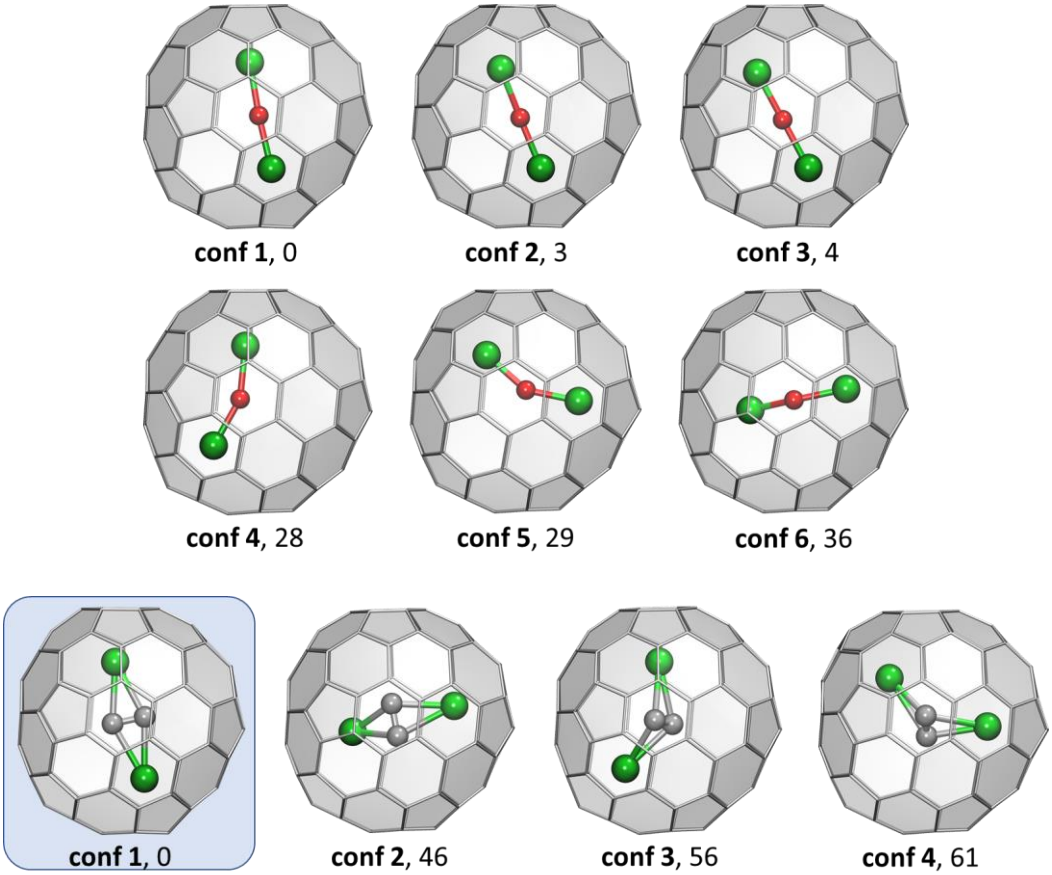

Figure S9c. DFT-optimized molecular structures of unique conformers of $Y_2O@C_s(32)$-C_{88} and $Y_2C_2@C_s(32)$-C_{88} with their relative energies (the number after comma, in kJ mol^{-1}). The conformer of $Y_2C_2@C_{88}$ corresponding to the site with the highest occupancy in SC-XRD structure of $Dy_2C_2@C_s(32)$-C_{88} is highlighted with light-blue background.

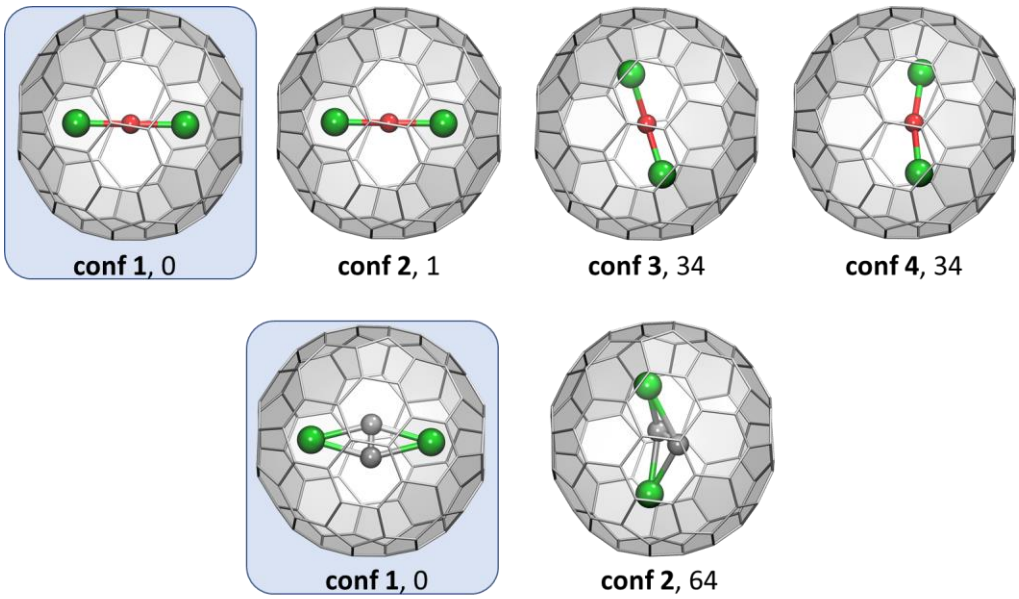

Figure S9d. DFT-optimized molecular structures of unique conformers of $Y_2O@D_2(35)$-C_{88} and $Y_2C_2@D_2(35)$-C_{88} with their relative energies (the number after comma, in kJ mol^{-1}). The conformers corresponding to the site with the highest occupancy in SC-XRD structure of $Dy_2O@D_2(35)$-C_{88} and $Dy_2C_2@D_2(35)$-C_{88} is highlighted with light-blue background. For $Y_2O@C_{88}$, conformers 2 and 3 are indistinguishable by eye but have slightly different position of the endohedral cluster.

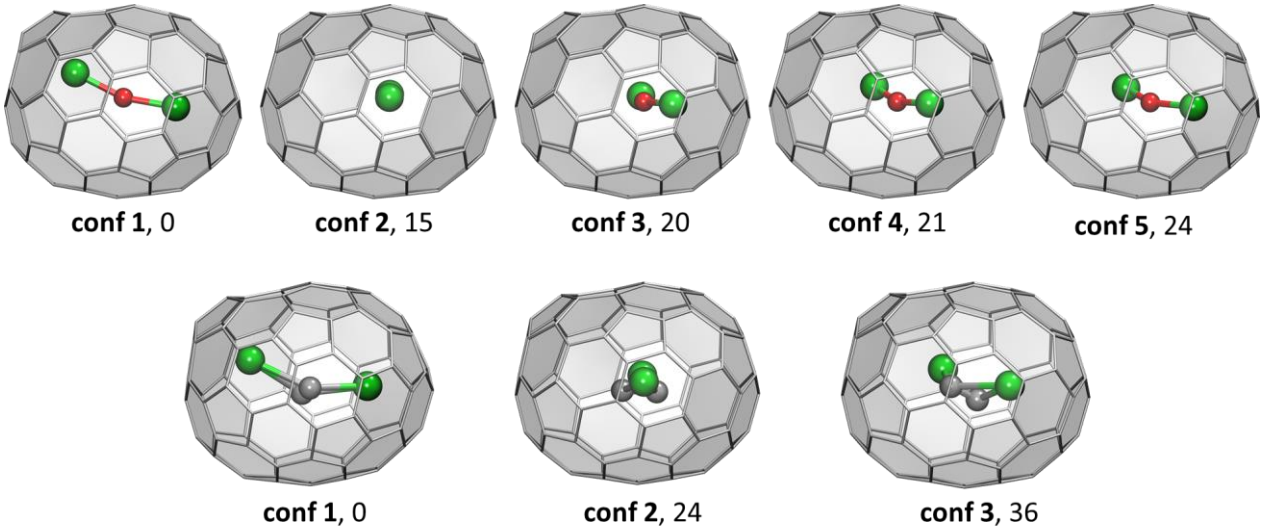

Figure S9e. DFT-optimized molecular structures of unique conformers of $Y_2O@C_s$(hept)-C_{88} and $Y_2C_2@C_s$(hept)-C_{88} with their relative energies (the number after comma, in kJ mol^{-1}).

Spectroscopic characterization

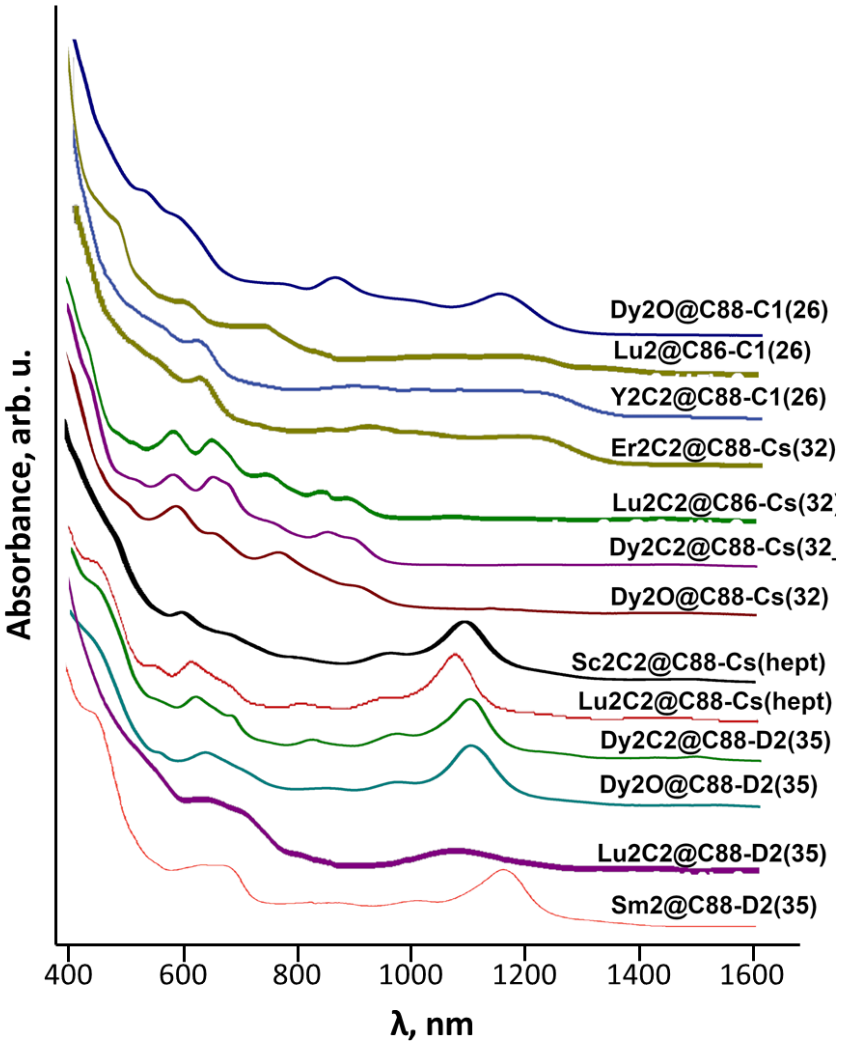

Figure S10. Comparison of Vis-NIR absorption spectra of various EMFs with C_{88} cages. See Table 1 in the main text for references to literature data.

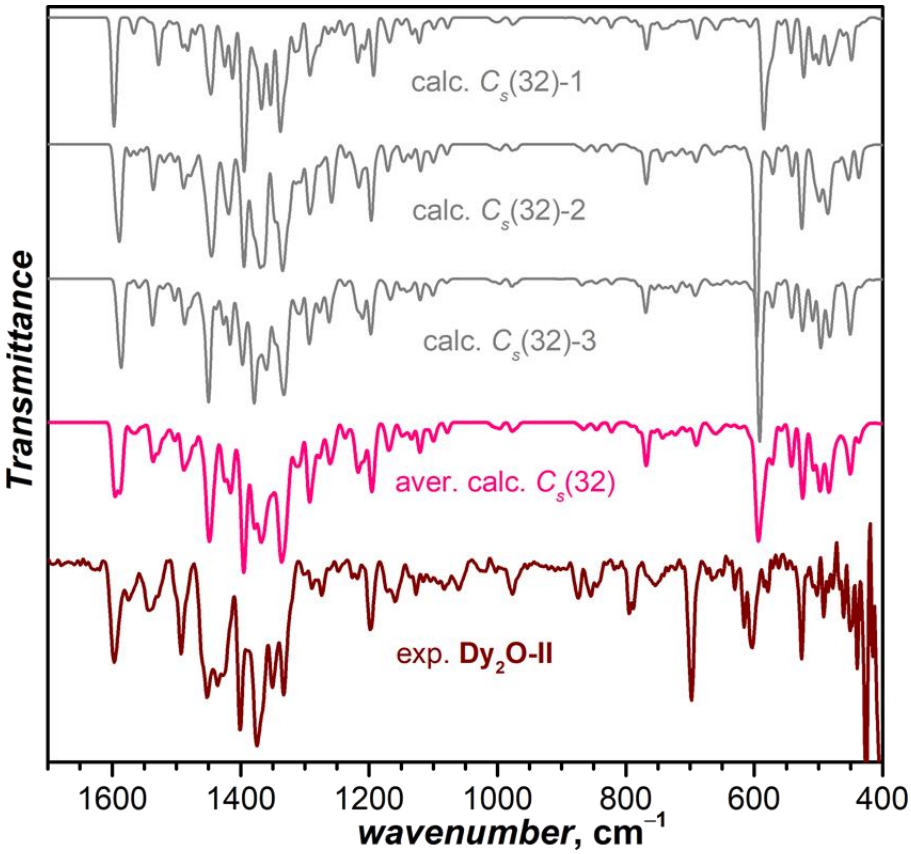

Figure S11. Experimental FT-IR spectrum of $Dy_2O@C_s(32)$-C_{88} compared to calculated spectra of three individual $Y_2O@C_s(32)$-C_{88} conformers and the averaged spectrum.

Ab initio calculations of the ligand-field splitting

Table S2a. Ligand-field splitting for Dy^{3+} ion in $Dy_2O@D_2(35)$-C_{88} computed at the CASSCF/RASSI level

	E, cm^{-1}	% composition in $\|m_J\rangle$ basis	g-tensor:		
			g_x	g_y	g_z
KD1	0.0	100.0 $\|\pm15/2\rangle$	0.000090	0.000170	19.901480
KD2	481.2	99.9 $\|\pm13/2\rangle$	0.007439	0.008720	16.996470
KD3	806.7	97.7 $\|\pm11/2\rangle$	0.099919	0.108452	14.210717
KD4	1030.1	94.3 $\|\pm9/2\rangle$, 4.8 $\|\pm5/2\rangle$	0.690779	0.787675	11.424669
KD5	1198.0	89.2 $\|\pm7/2\rangle$, 7.5 $\|\pm5/2\rangle$	1.014676	2.273010	8.650346
KD6	1319.7	77.4 $\|\pm5/2\rangle$, 14.8 $\|\pm1/2\rangle$, 4.3 $\|\pm9/2\rangle$	6.365486	2.262989	5.551419
KD7	1397.7	62.1 $\|\pm3/2\rangle$, 30.0 $\|\pm1/2\rangle$, 8.3 $\|\pm5/2\rangle$	12.972923	5.305683	2.097493
KD8	1493.9	61.8 $\|\pm1/2\rangle$, 27.0 $\|\pm3/2\rangle$, 8.9 $\|\pm5/2\rangle$	0.439425	19.222853	0.180391

Weight of individual-rank operators in the crystal field splitting:

$\hat{O}_2^q$:----------: 85.1 %

$\hat{O}_4^q$:----------: 9.4 %

$\hat{O}_6^q$:----------: 5.0 %

Table S2b. Ligand-field splitting for Dy^{3+} ion in $Dy_2C_2@D_2(35)$-C_{88} computed at the CASSCF/RASSI level

	E, cm^{-1}	% composition in $\|m_J\rangle$ basis	g-tensor:		
			g_x	g_y	g_z
KD1	0.0	99.8 $\|\pm15/2\rangle$	0.005037	0.007749	19.873248
KD2	224.4	86.5 $\|\pm13/2\rangle$, 10.6 $\|\pm9/2\rangle$	0.471914	1.023249	16.207817
KD3	299.2	74.8 $\|\pm11/2\rangle$, 21.0 $\|\pm7/2\rangle$	1.856945	1.104840	12.738305
KD4	390.2	66.8 $\|\pm9/2\rangle$, 17.0 $\|\pm5/2\rangle$, 12.6 $\|\pm13/2\rangle$	3.480845	0.343861	10.881521
KD5	509.4	59.0 $\|\pm7/2\rangle$, 22.1 $\|\pm11/2\rangle$, 15.4 $\|\pm3/2\rangle$	4.275675	0.093922	8.933248
KD6	599.4	55.2 $\|\pm5/2\rangle$, 20.1 $\|\pm1/2\rangle$, 16.7 $\|\pm9/2\rangle$	8.730022	3.620278	5.414610
KD7	679.1	49.3 $\|\pm3/2\rangle$, 22.7 $\|\pm1/2\rangle$, 13.1 $\|\pm7/2\rangle$, 12.6 $\|\pm5/2\rangle$	15.167529	3.309384	1.825401
KD8	779.7	55.0$\|\pm1/2\rangle$, 26.7 $\|\pm3/2\rangle$, 12.5 $\|\pm5/2\rangle$	0.405932	19.561048	0.192430

Weight of individual-rank operators in the crystal field splitting:

$\hat{O}_2^q$:----------: 77.6 %

$\hat{O}_4^q$:----------: 4.6 %

$\hat{O}_6^q$:----------: 16.9 %

Table S2c. Ligand-field splitting for Dy^{3+} ion in $Dy_2O@C_s(32)$-C_{88} computed at the CASSCF/RASSI level

	E, cm^{-1}	% composition in $\|m_J\rangle$ basis	g-tensor:		
			g_x	g_y	g_z
KD1	0.0	100.0 $\|\pm15/2\rangle$	0.000056	0.000075	19.902922
KD2	485.1	99.3 $\|\pm13/2\rangle$	0.005806	0.006768	17.019210
KD3	822.3	96.2 $\|\pm11/2\rangle$	0.094119	0.104556	14.209357
KD4	1057.0	91.7 $\|\pm9/2\rangle$, 4.8 $\|\pm5/2\rangle$	0.690931	0.753562	11.399485
KD5	1227.6	88.0 $\|\pm7/2\rangle$, 7.4 $\|\pm3/2\rangle$	1.272697	2.392225	8.822237
KD6	1347.6	81.3 $\|\pm5/2\rangle$, 10.2 $\|\pm1/2\rangle$, 4.7 $\|\pm9/2\rangle$	1.854033	1.943686	6.709584
KD7	1413.6	60.3 $\|\pm3/2\rangle$, 32.0 $\|\pm1/2\rangle$, 5.4 $\|\pm7/2\rangle$	9.659211	9.178826	2.500190
KD8	1505.2	57.4 $\|\pm1/2\rangle$, 29.3 $\|\pm3/2\rangle$, 10.7 $\|\pm5/2\rangle$	0.669296	19.084143	0.244336

Weight of individual-rank operators in the crystal field splitting:

$\hat{O}_2^q$:----------: 83.1 %

$\hat{O}_4^q$:----------: 9.9 %

$\hat{O}_6^q$:----------: 6.0 %

Table S2d. Ligand-field splitting for Dy^{3+} ion in $Dy_2C_2@C_s(32)$-C_{88} computed at the CASSCF/RASSI level

	E, cm^{-1}	% composition in $\|m_J\rangle$ basis	g-tensor:		
			g_x	g_y	g_z
KD1	0.0	99.1 $\|\pm15/2\rangle$	0.006877	0.011001	19.789050
KD2	156.7	86.2 $\|\pm13/2\rangle$, 6.3 $\|\pm9/2\rangle$	0.152384	0.272725	16.301342
KD3	281.1	70.9 $\|\pm11/2\rangle$, 14.7 $\|\pm7/2\rangle$, 5.4 $\|\pm9/2\rangle$	0.648486	0.483792	12.855024
KD4	435.9	55.0 $\|\pm9/2\rangle$, 19.4 $\|\pm5/2\rangle$, 12.4 $\|\pm13/2\rangle$	1.336312	0.321309	10.704763
KD5	589.4	34.7 $\|\pm3/2\rangle$, 33.2 $\|\pm7/2\rangle$, 22.7 $\|\pm11/2\rangle$	3.171949	1.815477	8.243343
KD6	668.5	53.6 $\|\pm1/2\rangle$, 19.5 $\|\pm9/2\rangle$, 16.7 $\|\pm5/2\rangle$, 9.7 $\|\pm7/2\rangle$	10.452485	6.974011	3.082671
KD7	746.5	31.8 $\|\pm5/2\rangle$, 26.8 $\|\pm3/2\rangle$, 24.9 $\|\pm7/2\rangle$, 9.0 $\|\pm9/2\rangle$	16.816910	0.530357	0.324811
KD8	872.5	31.5$\|\pm1/2\rangle$, 31.4 $\|\pm3/2\rangle$, 22.7 $\|\pm5/2\rangle$, 10.6 $\|\pm7/2\rangle$	19.595437	0.131556	0.073222

Weight of individual-rank operators in the crystal field splitting:

$\hat{O}_2^q$:----------: 72.5 %

$\hat{O}_4^q$:----------: 6.4 %

$\hat{O}_6^q$:----------: 19.3 %

Magnetic properties

In the lowest-energy part of the spectrum, the system of two Dy ions with strong axial ligand field gives two quasi-doublets with ferromagnetic (FM) and antiferromagnetic (AFM) alignment of Dy^{3+} magnetic moments (Fig. S12). Dy magnetic moments are not necessarily collinear, so both states may have non-zero magnetic moment equal (in μ_B) $g_z \sin(\alpha/2)$ and $g_z \cos(\alpha/2)$ (where g_z is pseudospin g-tensor describing single-ion ground state, Table S2). The state with a smaller moment is considered to be AFM, and the one with the larger moment is FM. These states can be described using the effective spin Hamiltonian used in this work:

$$\hat{H}_{\mathrm{spin}} = \hat{H}_{\mathrm{LF}_1} + \hat{H}_{\mathrm{LF}_2} - 2j_{12}\hat{J}_1 \cdot \hat{J}_2 + \hat{H}_{\mathrm{ZEE}} \qquad (1)$$

where $\hat{H}_{\mathrm{LF_i}}$ are single-ion ligand-field Hamiltonians of Dy^{3+}, j_{12} is the coupling constant between dysprosium moments, and $\hat{H}_{\mathrm{ZEE}}$ is the Zeeman term describing interaction of Dy^{3+} magnetic moments with the external magnetic field. In essence, this Hamiltonian uses single-ion ligand field ($\hat{H}_{\mathrm{LF'}}$) terms to split Dy^{3+} multiplets into LF states (Table S2), and then adds interactions between individual LF states in a bilinear form with effective constant j_{12}, which includes both exchange and dipolar interactions. We use *ab initio* computed ligand field parameters in $\hat{H}_{\mathrm{LF_i}}$, and Dy^{3+} moments $\hat{J}_{\mathrm{i}}$ are treated in the $|J, m_J\rangle$ basis sets of the $^6H_{15/2}$ multiplet.

In the low-energy part of the spectrum, the Hamiltonian gives two quasi-doublets formed by coupling of the ground state KDs of two ions (KD1 and KD1') with ferromagnetic (FM) and antiferromagnetic (AFM) alignment of magnetic moments (Fig. S12). The energies of these two quasi-doublets will be:

$$E_{\mathrm{FM}} = -2J_{z1}J_{z2}j_{12}\cos(\alpha)$$

$$E_{\mathrm{AFM}} = 2J_{z1}J_{z2}j_{12}\cos(\alpha)$$

where J_{z1} and J_{z2} are J_z projections of J_1 and J_2 in the ground state KDs of Dy^{3+} ions onto their individual quantization axes, α is the angle between these quantization axes, and the LF terms are neglected since they are the same for both states. Therefore, the energy difference between AFM and FM states is:

$$\Delta E_{\mathrm{AFM-FM}} = 4J_{z1}J_{z2}j_{12}\cos(\alpha) \approx 225 j_{12}\cos(\alpha),$$

The last approximate term is because in the ground state KDs of Dy^{3+} ions, $J_{zi} \approx 15/2$.

The spectrum of the Hamiltonian also includes higher-energy states resulting from the interaction of excited LF states of single ions, but if the LF splitting is large, these will have noticeable contribution only at high temperatures.

The Hamiltonian (1) was used in the fitting of experimental magnetization curves. In the fitting, j_{12} and α were treated as free parameters, and computed curves were powder-averaged to be compatible with experimental magnetization curves measured for powder samples. Only experimental points in the field range where hysteresis is very narrow or completely closed were used as Hamiltonian (1) describes only magnetization in equilibrium and hence cannot be used to model magnetic hysteresis. In Fig. S13, experimental magnetization curves are compared to results of simulations with fitted parameters. The same fitted parameters were then used to simulate χT curves shown in Fig. 6 in the main text.

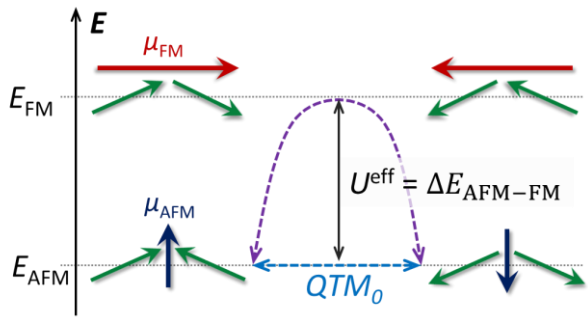

Figure S12. Schematic description of two quasi-doublets in the low-energy part of the energy of a $\{Dy_2\}$ system with Ising-type Dy^{3+} moments. Green arrows denote magnetic moments of individual Dy^{3+} ions (≈10 μ_B each), red and blue arrows are magnetic moments of coupled states ($\mu_{\mathrm{AFM}} = g_z \sin(\alpha/2)\mu_{\mathrm{B}}$; $\mu_{\mathrm{FM}} = g_z \cos(\alpha/2)\mu_{\mathrm{B}}$). Dashed arrows are relaxation pathways (zero field QTM_0, and Orbach process with the barrier equal $\Delta E_{\mathrm{AFM-FM}}$).

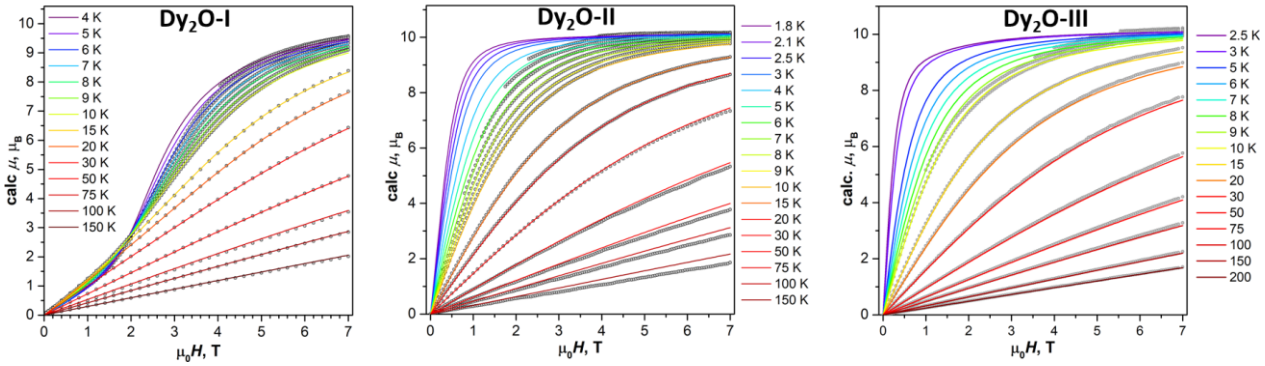

Figure S13a. Experimental (dots) and fitted (colored lines) magnetization curves of $Dy_2O@C_{88}$ isomers (**Dy_2O-I** is $Dy_2O@C_1(26)$-C_{88}, **Dy_2O-II** is $Dy_2O@C_s(32)$-C_{88}, **Dy_2O-III** is $Dy_2O@D_2(35)$-C_{88}). Note that at low temperature, only high-field experimental points were used in fitting since at lower field the hysteresis was open.

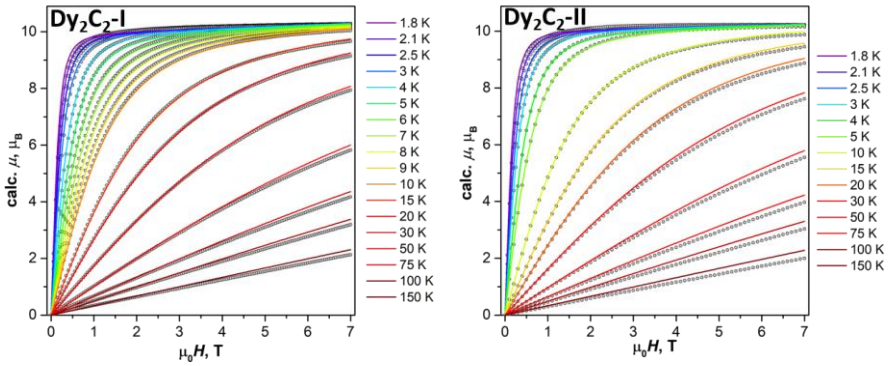

Figure S13b. Experimental (dots) and fitted (colored lines) magnetization curves of $Dy_2C_2@C_{88}$ isomers (**Dy_2C_2-I** is $Dy_2C_2@C_s(32)$-C_{88}, **Dy_2C_2-II** is $Dy_2C_2@D_2(35)$-C_{88}).

Magnetization relaxation times

Magnetization decay curves were measured after the samples were first magnetized at 7 Tesla and then the field was quickly ramped to 0 T ($Dy_2O@C_1(26)$-C_{88} and $Dy_2O@D_2(35)$-C_{88}) or 0.2 T ($Dy_2O@C_s(32)$-C_{88}). The decay curves were fitted with stretched exponential function:

$$M(t) = M_{eq} + (M_0 - M_{eq}) \exp\left[-\left(\frac{t}{\tau_M}\right)^{\beta}\right]$$

Where M_{eq} and M_0 are the equilibrium and initial magnetizations, respectively, τ_M is a characteristic relaxation time and β is a parameter, characterizing distribution of relaxation rates in the sample. For a single-exponential decay, β = 1. For long relaxation times, such as observed for $Dy_2O@C_1(26)$-C_{88} at low temperatures, reliable determination of τ_M requires unfeasibly long measurements because the fitted value is strongly related to M_{eq}. To circumvent this problem, we fixed M_{eq} = 0 in such fits since the measurements were performed in zero field, at which equilibrium magnetization is zero.

Examples of decay curves with their fitting are presented in Figure S14-S16. The values of τ_M and β determined in the fits are listed in Tables S3-S5.

Table S3. Magnetization relaxation times τ_M of $Dy_2O@C_1(26)$-C_{88} measured at different temperatures

T, K	τ_M, s @ 0 T	β
1.8	58008	0.58
2	41807	0.59
2.2	26446	0.60
2.5	11676	0.63
2.65	7676	0.64
2.85	4632	0.61
3.1	2579	0.63
3.3	1484	0.66
3.5	1233	0.60
3.65	927	0.62
4	506	0.66
4.45	290	0.60
5	178	0.58
5.7	139	0.62
6.5	82	0.65

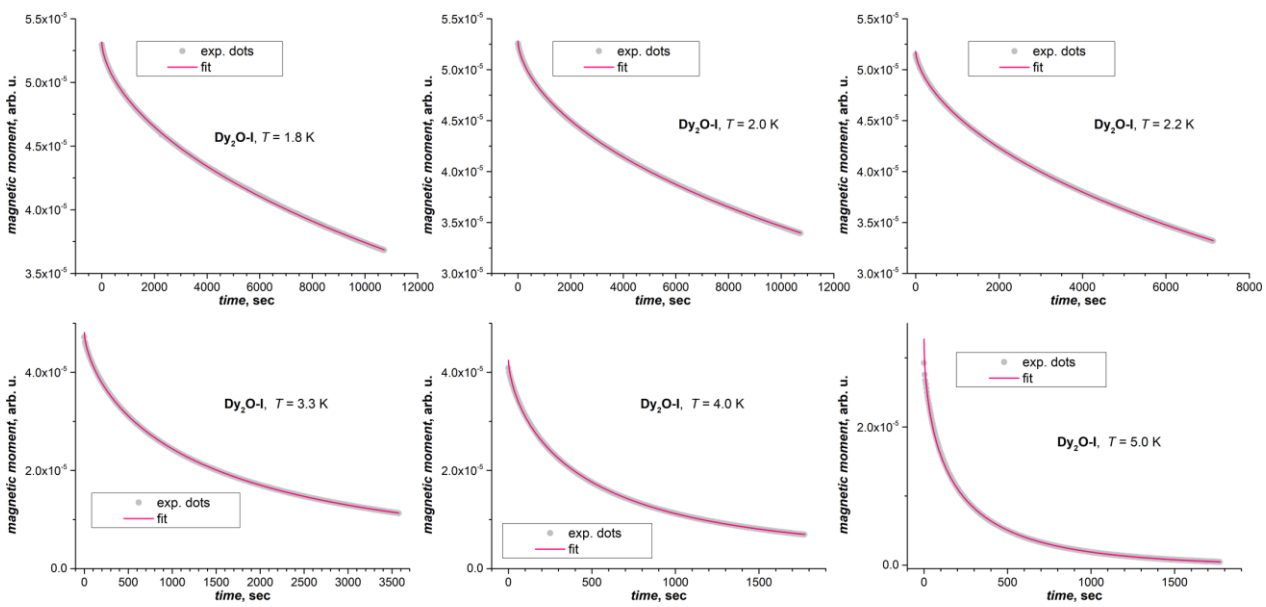

Figure S14. Representative magnetization decay curves measured for $Dy_2O@C_1(26)$-C_{88} and their fitting with stretched exponential function.

Table S4. Magnetization relaxation times τ_M of $Dy_2O@C_s(32)$-C_{88} measured at different temperatures at 0.2 T

T, K	τ_M, s @ 0.2 T	β
1.8	1535	0.59
1.9	1364	0.59
2	1200	0.58
2.1	1059	0.57
2.2	921	0.59
2.35	749	0.58
2.5	611	0.58
2.65	498	0.58
2.8	409	0.59
3	324	0.58
3.3	252	0.59
3.6	194	0.59
4	152	0.60
4.3	125	0.62
4.6	107	0.64
5	84	0.67

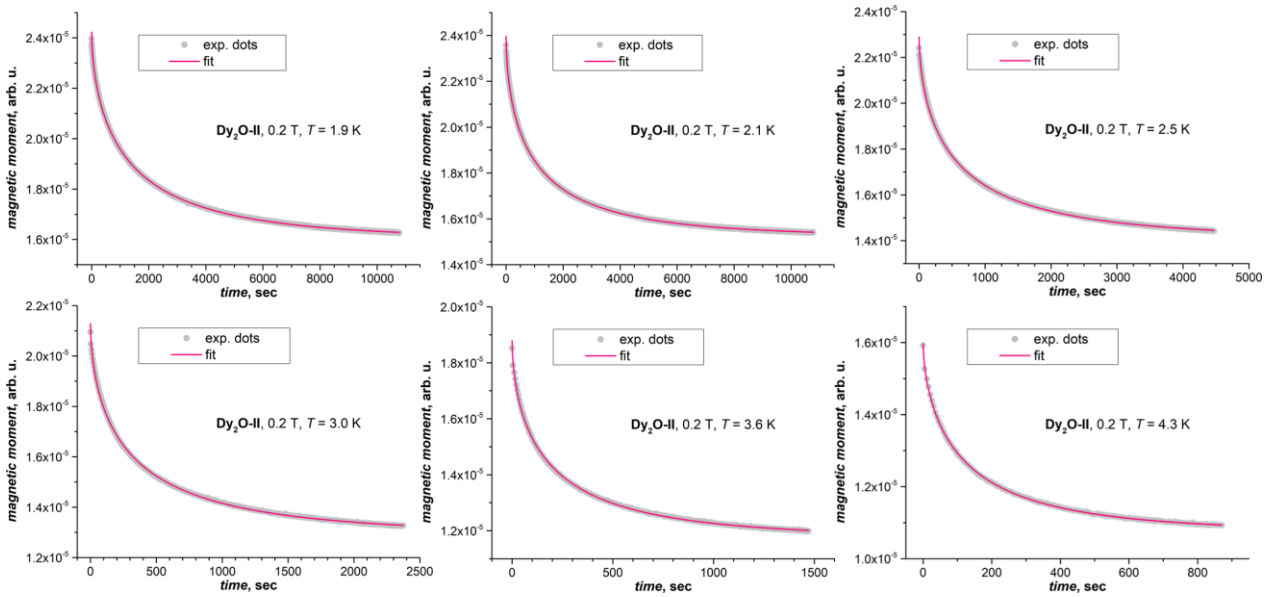

Figure S15. Representative magnetization decay curves measured for $Dy_2O@C_s(32)$-C_{88} in the field of 0.2 T and their fitting with stretched exponential function.

Table S5. Magnetization relaxation times τ_M of $Dy_2O@D_2(35)$-C_{88} measured at different temperatures

T, K	τ_M, s @ 0 T	β
1.8	1794	0.63
1.9	1406	0.62
2	1122	0.62
2.2	781	0.62
2.4	573	0.62
2.6	419	0.61
2.8	330	0.62
3.1	228	0.61
3.4	173	0.65
3.7	119	0.62
4	83	0.63
4.5	59	0.65

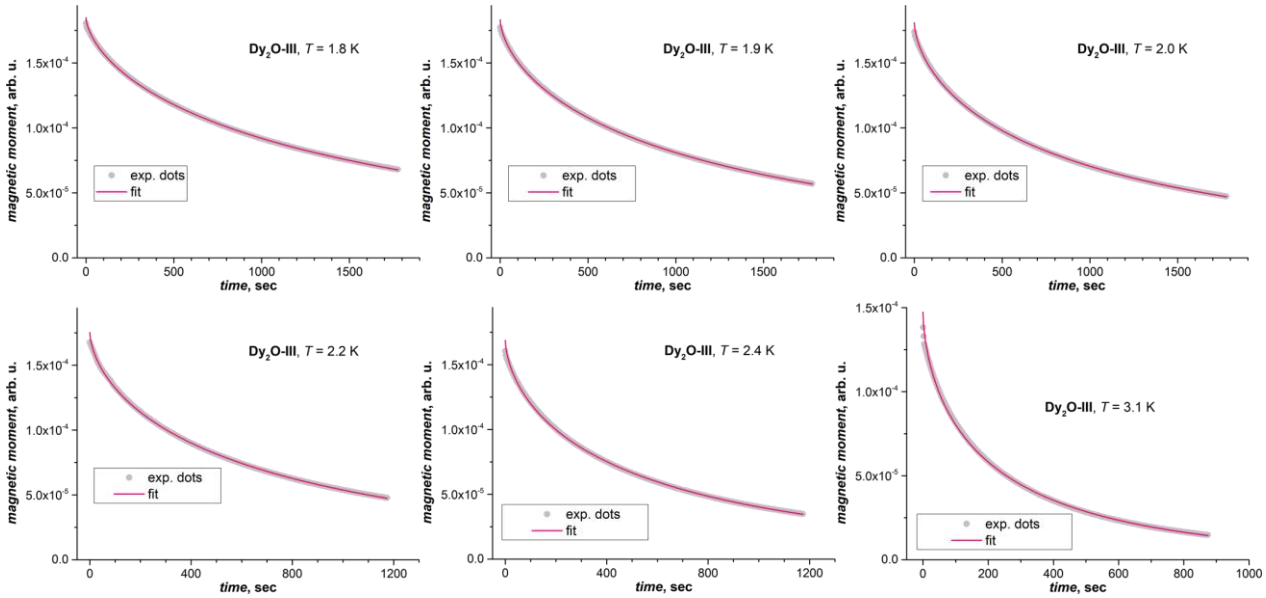

Figure S16. Representative magnetization decay curves measured for $Dy_2O@D_2(35)$-C_{88} and their fitting with stretched exponential function.

References

1. U. Mueller, R. Förster, M. Hellmig, F. U. Huschmann, A. Kastner, P. Malecki, S. Pühringer, M. Röwer, K. Sparta, M. Steffien, M. Ühlein, P. Wilk and M. S. Weiss, *Eur. Phys. J. Plus*, 2015, **130**, 141.
2. W. Kabsch, *Acta Cryst. D*, 2010, **66**, 125-132.
3. K. M. Sparta, M. Krug, U. Heinemann, U. Mueller and M. S. Weiss, *J. Appl. Crystallogr.*, 2016, **49**, 1085-1092.
4. G. Sheldrick, *Acta Cryst. C*, 2015, **71**, 3-8.
5. N. F. Chilton, R. P. Anderson, L. D. Turner, A. Soncini and K. S. Murray, *J. Comput. Chem.*, 2013, **34**, 1164-1175.
6. D. N. Laikov and Y. A. Ustynuk, *Russ. Chem. Bull.*, 2005, **54**, 820-826.
7. D. N. Laikov, *Chem. Phys. Lett.*, 1997, **281**, 151-156.
8. J. Hafner, *J. Comput. Chem.*, 2008, **29**, 2044-2078.
9. G. Kresse and J. Hafner, *Phys. Rev. B*, 1993, **47**, 558-561.
10. G. Kresse and D. Joubert, *Phys. Rev. B*, 1999, **59**, 1758-1775.
11. J. P. Perdew, K. Burke and M. Ernzerhof, *Phys. Rev. Lett.*, 1996, **77**, 3865-3868.
12. S. Grimme, *WIREs Comput. Mol. Sci.*, 2011, **1**, 211-228.
13. F. Aquilante, J. Autschbach, A. Baiardi, S. Battaglia, V. A. Borin, L. F. Chibotaru, I. Conti, L. D. Vico, M. Delcey, I. F. Galván, N. Ferré, L. Freitag, M. Garavelli, X. Gong, S. Knecht, E. D. Larsson, R. Lindh, M. Lundberg, P. Å. Malmqvist, A. Nenov, J. Norell, M. Odelius, M. Olivucci, T. B. Pedersen, L. Pedraza-González, Q. M. Phung, K. Pierloot, M. Reiher, I. Schapiro, J. Segarra-Martí, F. Segatta, L. Seijo, S. Sen, D.-C. Sergentu, C. J. Stein, L. Ungur, M. Vacher, A. Valentini and V. Veryazov, *J. Chem. Phys.*, 2020, **152**, 214117.
14. L. F. Chibotaru and L. Ungur, *J. Chem. Phys.*, 2012, **137**, 064112.